Title

Soft Somatosensitive Actuators via Embedded 3D Printing

Journal

Advanced Materials, 30(15)

ISSN

0935-9648

Authors

Truby, Ryan L

Wehner, Michael

Grosskopf, Abigail K

et al.

Publication Date

2018-04-01

DOI

10.1002/adma.201706383

ADVANCED MATERIALS
www.advmat.de

Soft Somatosensitive Actuators via Embedded 3D Printing

Ryan L. Truby, Michael Wehner, Abigail K. Grosskopf, Daniel M. Vogt, Sebastien G. M. Uzel, Robert J. Wood, and Jennifer A. Lewis**

Humans possess manual dexterity, motor skills, and other physical abilities that rely on feedback provided by the somatosensory system. Herein, a method is reported for creating soft somatosensitive actuators (SSAs) via embedded 3D printing, which are innervated with multiple conductive features that simultaneously enable haptic, proprioceptive, and thermoceptive sensing. This novel manufacturing approach enables the seamless integration of multiple ionically conductive and fluidic features within elastomeric matrices to produce SSAs with the desired bioinspired sensing and actuation capabilities. Each printed sensor is composed of an ionically conductive gel that exhibits both long-term stability and hysteresis-free performance. As an exemplar, multiple SSAs are combined into a soft robotic gripper that provides proprioceptive and haptic feedback via embedded curvature, inflation, and contact sensors, including deep and fine touch contact sensors. The multimaterial manufacturing platform enables complex sensing motifs to be easily integrated into soft actuating systems, which is a necessary step toward closed-loop feedback control of soft robots, machines, and haptic devices.

Humans possess manual dexterity, motor skills, and other physical abilities that rely on feedback provided by the specialized receptors and afferent neurons that comprise our somatosensory system. The emerging field of soft robotics has strived to replicate these capabilities for myriad applications,[1,2] including universal[3] and compliant end effectors for robotic handling,[4–6] wearable devices for rehabilitation and performance enhancement,[7–9] robust systems that operate in extreme environments,[10–13] and autonomous soft robots.[10–12,14,15] However, to realize their full potential, next-generation soft robots require integrated soft sensors that provide discrete, somatosensory feedback motifs, including proprioceptive, haptic, and thermoceptive sensing.[1,2,16]

Molded and laminated elastomers with embedded pneumatic networks are widely used materials for soft robots.[1,2,16] Recent efforts have focused on introducing sensing capabilities within these fluidic elastomer actuators (FEAs).[5,6,17–22] However, to date, most embodiments provide only a single mode of feedback that is achieved by integrating conventional rigid sensors[23–25] or soft sensors composed of conductive liquid metals,[5,18,20,26,27] aqueous ionic conductors,[19,21] or conductive nanoparticle-filled polymer composites.[17,22,28] FEAs that provide multiple modes of sensory feedback have recently been reported.[5,6,26] Most notably, FEAs with proprioception and exteroceptive contact sensing have been achieved by incorporating either multiple liquid metal sensors[5,26] or elastomeric waveguides that provide feedback through optical power loss during waveguide deformation.[6] However, their fabrication requires multiple molding and lamination steps that constrain their overall complexity and sensing capabilities. Embodiments that rely on ionically conductive sensing pose additional challenges, including sensor failure due to water evaporation,[29–31] while those based on conductive nanoparticle-filled polymers exhibit hysteresis as their particle network is disrupted during large, repeated deformations.[32,33]

Here, we report a method for creating soft robotic actuators innervated with a complex network of sensors, referred to as soft somatosensitive actuators (SSAs), via multimaterial, embedded 3D (EMB3D) printing.[14,34–36] This manufacturing approach enables the seamless integration of multiple ionically conductive and fluidic features within elastomeric matrices to create SSAs with the desired bioinspired sensing and actuation capabilities. By assembling three SSAs into a soft robotic gripper, we specifically demonstrate proprioceptive and haptic feedback enabled by embedded curvature, inflation, and contact sensors. Harnessing the temperature-dependent ionic conductivity[37,38] of the SSAs' contact sensors coupled with our free-form fabrication process, we also created SSAs with temperature and deep-versus-fine touch contact sensing, respectively, which have not yet been realized by other soft robotic actuators.

Dr. R. L. Truby, A. K. Grosskopf, Dr. S. G. M. Uzel, Prof. J. A. Lewis
John A. Paulson School of Engineering and Applied Sciences
Wyss Institute for Biologically Inspired Engineering
Harvard University
Pierce Hall Rm 211, 29 Oxford Street, Cambridge, MA 02138, USA
E-mail: jalewis@seas.harvard.edu
Prof. M. Wehner
Department of Computer Engineering
University of California Santa Cruz
1156 High Street, MS:SOE3, Santa Cruz, CA 95064, USA
D. M. Vogt, Prof. R. J. Wood
John A. Paulson School of Engineering and Applied Sciences
Wyss Institute for Biologically Inspired Engineering
Harvard University
60 Oxford Street, Cambridge, MA 02138, USA
E-mail: rjwood@seas.harvard.edu
The ORCID identification number(s) for the author(s) of this article can be found under https://doi.org/10.1002/adma.201706383.

DOI: 10.1002/adma.201706383

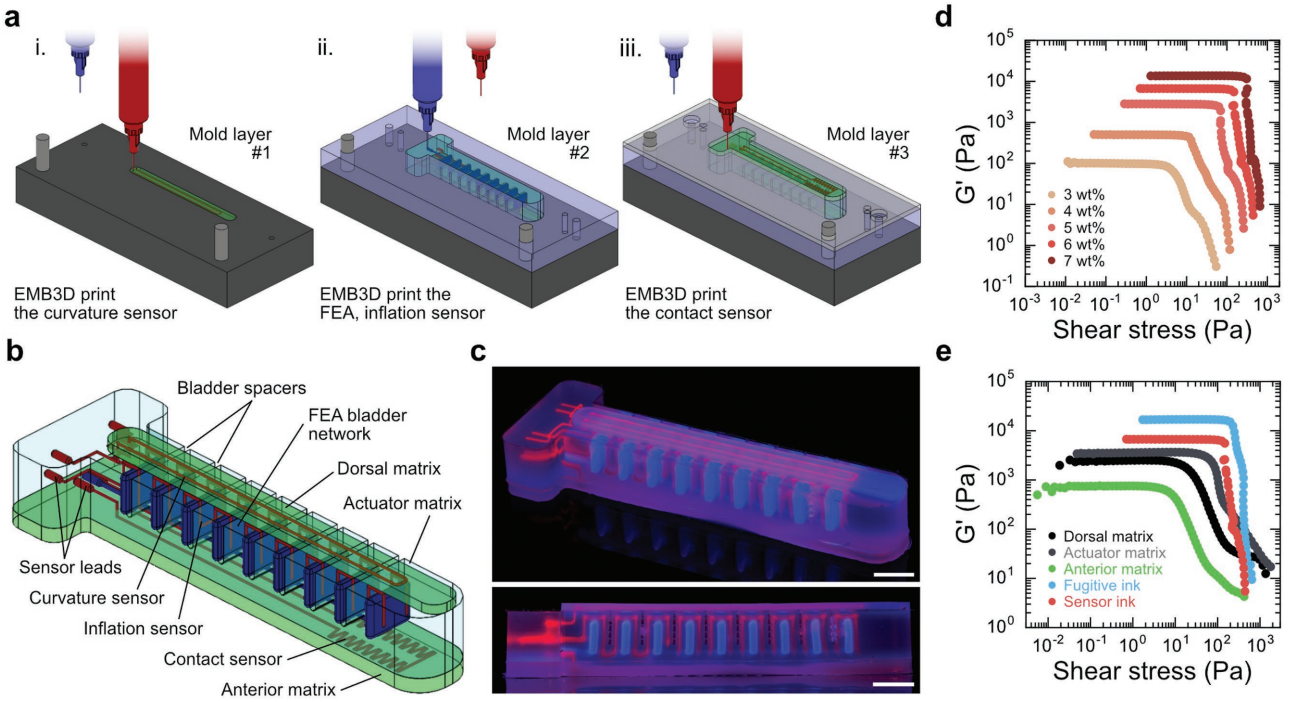

Figure 1. Fabrication of soft somatosensitive actuator (SSA) innervated with multiple soft sensors. a) The curvature sensor is printed within the dorsal matrix (Layer 1); the actuator features and inflation sensor are printed within the actuator matrix (Layer 2); and the contact sensor is printed in the anterior matrix (Layer 3). b) Schematic illustrations and c) images of the final SSA. The images in (c) are taken under black light exposure, and the fugitive (blue) and sensor (red) inks have been fluorescently dyed to facilitate visualization (scale bars are 10 mm). d) Log–log plot of storage modulus, G', as a function of shear stress for sensor inks composed of 1-ethyl-3-methylimidazolium ethyl sulfate with varying fumed silica content (wt%). e) Log–log plot of G' as a function of shear stress for all matrix materials and inks used for constructing these SSAs via EMB3D printing.

The SSAs are fabricated by directly writing the sensing and fluidic networks within molded elastomeric matrices via multimaterial, EMB3D printing (**Figure 1**). Specifically, conductive ionogel and fugitive inks are printed within three elastomeric matrices—the dorsal, actuator, and anterior matrix materials—to define the sensor and pneumatic networks required for sensing and actuation, respectively. The key steps for EMB3D printing of SSAs are highlighted in Figure 1a (see Figure S1 in the Supporting Information for additional details). Briefly, the dorsal, actuator, and anterior matrix materials are loaded sequentially in the mold and the following features are printed: (i) the curvature sensor in the dorsal matrix, (ii) the FEA features (including actuator spacers and bladder network) and inflation sensor in the actuator matrix, and (iii) the contact sensor in the anterior matrix. All sensor leads terminate in the actuator matrix. After printing, the matrix materials are cured and the fully fabricated SSA (Figure 1b,c and Figure S2, Supporting Information) is removed from the mold assembly. Next, the fugitive ink is evacuated from the SSA leaving behind an open network of pneumatic channels (see the Experimental Section), and electrical leads are inserted into the sensors. Each SSA bends freely in a semi-circular motif when inflated, and the inflation, curvature, and contact sensors directly embedded within the body of the SSA are designed to deform, and consequently increase in resistance, when the SSA inflates, bends, and makes contact with external bodies, respectively.

Each elastomeric matrix must possess the requisite rheological properties for EMB3D printing as well as the appropriate mechanical properties upon curing. Prior to curing, they exhibit shear thinning and thixotropic behavior (Figure S3, Supporting Information), which facilitates their flow into each mold as well as the integration of functional features via EMB3D printing.[14] Upon curing, the dorsal matrix consists of a highly extensible elastomer (Shore-00 Hardness of 10) that exhibits minimal impedance on SSA bending. The actuator matrix exhibits the highest durometer (Shore-A Harness of 40) to enable appropriate force generation, while the anterior matrix consists of an elastomer with an intermediate durometer (Shore-00 Hardness of 30).

The sensor ink is a conductive ionogel composed of the organic ionic liquid 1-ethyl-3-methylimidazolium ethyl sulfate (EMIM-ES) filled with fumed silica particles, which serve as a rheology modifier. With their low vapor pressure, nonpermeability through elastomeric matrices, and appropriate resistivity for sensing applications, organic ionic liquids have been used previously as sensors in soft robots.[39,40] To introduce those sensors, an ionic liquid is injected into channels within elastomeric structures produced by multi-step molding and lamination methods.[39,40] By adding fumed silica nanoparticles to this Newtonian fluid, we created a conductive ionogel that exhibits shear-thinning behavior (Figure S4a, Supporting Information) and a shear yield stress, τ_y, that increases with filler concentration (Figure 1d). The optimal ionogel for EMB3D printing contains 6 wt% fumed silica particles, which gives rise to τ_y = ≈150 Pa. The fugitive ink used to print the pneumatic features within these SSAs is composed of an aqueous gel of Pluronic F127, a poly(ethylene oxide)-*b*-poly(propylene oxide)-*b*-poly(ethylene

oxide) triblock copolymer.[14,34,41] The rheological behavior of the three matrix materials and two inks used to construct the SSAs are shown in Figure 1e and Figure S4b (Supporting Information).

Each sensor consists of a resistive strain gauge whose electrical resistance is given by $R = \rho L/A$, where ρ is the resistivity, L is the length, and A is the cross-sectional area of the printed ionogel features. Low-voltage AC readout electronics are used to measure R without complications arising from capacitive charge separation or electrochemical reactions (see Figure S5 in the Supporting Information).[29] The change in resistance, ΔR, during operation is given by $\Delta R = R - R_0$, where R_0 is the initial resistance. We first probed the effect of relative humidity (RH) on R by creating a model sensor embedded within the anterior matrix (Figure S6, Supporting Information), since the hygroscopic sensor ink uptakes water that permeates through the crosslinked matrices. We observed decreases in R over time that can be attributed partially to increases in cross-sectional area, A, due to swelling by water uptake (Figure S6c, Supporting Information) and the concomitant decrease in ρ in these ionogel–water mixtures.[42] After 4 d, we find that the sensors reach a steady R value that changes negligibly over time.

Next, we characterized ΔR for the embedded curvature, inflation, and contact sensors during free and blocked displacement as well as the ΔR of the contact sensor during the application of a contact pressure (Figure S7, Supporting Information). When inflated, the bladders within the SSAs compress the inflation sensor (i.e., A decreases) and elongate the curvature sensor (i.e., L increases) during bending. As shown in **Figure 2**a, for

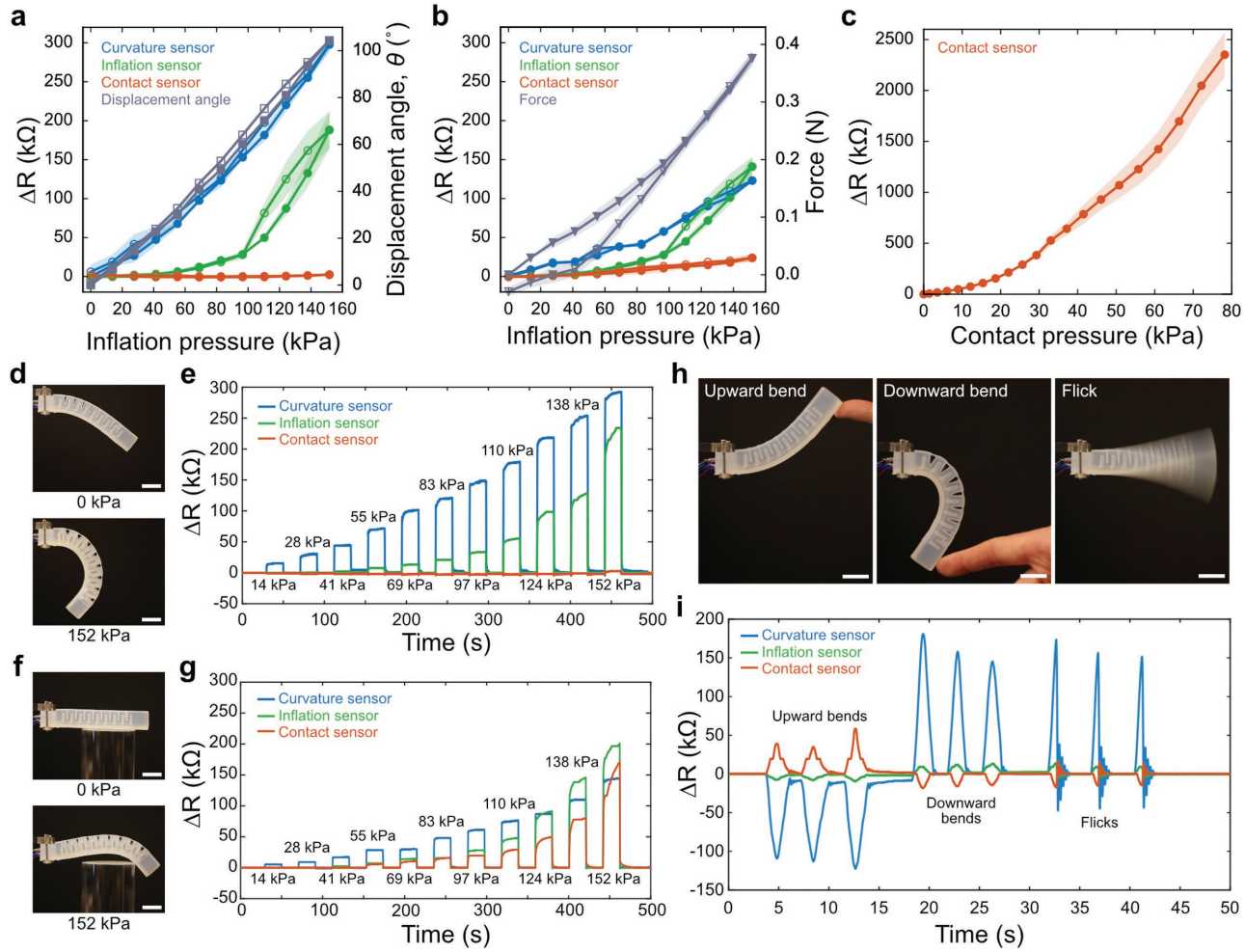

Figure 2. Performance of soft somatosensitive actuators. a) Resistance change, ΔR, for the curvature, inflation, and contact sensors and displacement angle, θ, as a function of inflation pressure during free displacement. b) ΔR for each sensor and force generated as a function of inflation pressure during blocked displacement. c) $\Delta R_{contact}$ as a function of applied contact pressure. For (a)–(c), data points and shaded regions represent mean values and standard deviations, respectively, ($n = 3$). d) Images of an SSA at 0 kPa (top) and 152 kPa (bottom) during a dynamic free displacement test, in which the SSA experiences periods of no inflation (0 kPa for 20 s) to increasing inflation pressure (held for 20 s) in increments of 14–152 kPa. e) ΔR of each sensor is plotted as a function of time. f) Still images of an SSA inflating against an acrylic rod at 0 kPa (top) and 152 kPa (bottom) during a dynamic blocked displacement test, in which the SSA is actuated via the same inflation sequence as in (d) and (e). g) ΔR for each sensor is plotted as a function of time. h) Upward bend (left), downward bend (middle), and flick-style (right) manipulations carried out on a noninflated SSA. i) ΔR for each sensor is plotted as a function of time for an SSA undergoing a sequence of three upward bends, three downward bends, and three flicks. All scale bars are 20 mm.

a freely bending SSA, $\Delta R_{curvature}$, $\Delta R_{inflation}$, and displacement angle, θ, all increase with inflation pressure, while $\Delta R_{contact}$ negligibly changes. During blocked displacement, the SSA cannot bend freely when inflated against a rigid obstruction. Correspondingly, $\Delta R_{curvature}$, $\Delta R_{inflation}$, and $\Delta R_{contact}$ all increase, but not in an identical manner as in free displacement: at each respective inflation pressure, $\Delta R_{curvature}$ is noticeably less due to obstructed bending, $\Delta R_{inflation}$ is slightly lower, and $\Delta R_{contact}$ is only slightly positive compared to free displacement values. Using a mass balance as our obstruction, we find increasing inflation pressure drives increased force generation (Figure 2b). The representative SSA characterized in Figure 2 is capable of generating blocked forces of 0.38 +/− 0.01 N at an inflation pressure of 152 kPa. Finally, $\Delta R_{contact}$ noticeably changes when contact pressures are directly applied to the distal meander of the contact sensor (Figure 2c). Similar to observations reported for liquid metal-based soft sensors,[43] we find that $\Delta R_{inflation}$ and $\Delta R_{contact}$ are nonlinearly related to inflation and contact pressures, respectively, while $\Delta R_{curvature}$ increases linearly with inflation pressure.

A slight hysteresis in $\Delta R_{curvature}$ and $\Delta R_{inflation}$ is observed in the ΔR readouts over inflation–deflation cycles. We believe this arises from the viscoelastic nature of the elastomeric matrices within the SSA, since it is also observed in liquid metal-based soft sensors.[43,44] This hypothesis is further supported by the sensors' ΔR recorded during dynamic free (Figure 2d, e and Movie S1, Supporting Information) and blocked (Figure 2f,g and Movie S2, Supporting Information) displacement trials, in which the SSA undergoes repeated deflation–inflation cycles at 20 s intervals and inflation pressure increases at 14 kPa increments. The readout data in Figure 2e,g agree well with the data reported in Figure 2a,b, respectively, and ΔR for each sensor nearly returns to zero once the SSA is deflated. In the dynamic blocked displacement trial, the SSA is placed on a rigid acrylic rod such that the rod edge provides contact pressures that produce clear increases in $\Delta R_{contact}$ at higher inflation pressures (Figure 2g).

We explored readouts from three simple external manipulation motifs on noninflated SSAs (Figure 2h and Movie S3, Supporting Information). Figure 2i shows ΔR for each sensor with time during three upward bends, three downward bends, and three flicks. $\Delta R_{inflation}$ is negligible, since the SSA is not inflated. During upward bending, the contact and curvature sensors lay above and beneath the neutral axis of the SSA, respectively. Hence, the contact sensor elongates, while the curvature sensor is compressed, i.e., $\Delta R_{contact} > 0$ and $\Delta R_{curvature} < 0$. During downward bending, the opposite responses are observed, i.e., $\Delta R_{contact} < 0$ and $\Delta R_{curvature} > 0$. During a flick-type deformation, $\Delta R_{contact}$ and $\Delta R_{curvature}$ mimic the response of a damped harmonic oscillator (Figure S8a, Supporting Information). Interestingly, this same behavior (Figure 2i) is also observed for an inflated SSA (Figure S8b and Movie S4, Supporting Information). The above data illustrate that the curvature, inflation, and contact sensors embedded within these SSAs provide the desired somatosensory feedback. The curvature sensor correlates with actuator displacement, the inflation sensor indicates whether or not the displacement is intentional, and the contact sensor indicates when it is in contact with an object. These sensors perform reliably even after six months of storing the SSAs under ambient conditions (Figure S9, Supporting Information).

To fully demonstrate the utility of this collective somatosensory feedback in a soft robotic system, we integrated three SSAs in a mounting assembly to produce a soft robotic gripper. For these demos, in which the gripper grabs various balls, all three SSAs are inflated identically, and the sensory feedback is collected only from the SSA in the center of the image shown in **Figure 3**. Figure 3a,b contains images and a corresponding plot of ΔR with time recorded from all sensors, respectively, during a simple object manipulation event (Movie S5, Supporting Information). Starting with a noninflated gripper, the ball is first used to bend the center SSA in an upward then downward manner to simulate interaction with an incoming object. The gripper is then inflated at a modest pressure of 55 kPa to grab the ball. At this inflation pressure, only an obvious increase in $\Delta R_{curvature}$ was anticipated, though $\Delta R_{inflation}$ and $\Delta R_{contact}$ slightly increased. Tugging the ball induces slight variations in $\Delta R_{curvature}$. At ≈22 s, the inflation pressure is increased to 152 kPa, leading to a concomitant rise in ΔR of each sensor. Now that the ball is tightly grabbed, clear changes are observed in $\Delta R_{curvature}$ and $\Delta R_{contact}$ when the ball is tugged again. The ball is pulled completely from the gripper at t = ≈34 s while the inflation pressure is maintained. Without the ball, the SSAs are able to more freely displace, increasing $\Delta R_{curvature}$ and decreasing $\Delta R_{contact}$ to ≈0 kΩ. We clearly observe the kinesthetic nature of the inflation sensor by removing the ball from the inflated gripper, as $\Delta R_{inflation}$ remains somewhat constant. R for all sensors returned to ≈R_0 once the SSAs were deflated.

Contact pressures generated by grabbing this first ball are rarely sufficient to create $\Delta R_{contact}$ > ≈100 kΩ. This is a consequence of the overall design as well as the materials used in these SSAs. By grabbing objects with different textures that create higher contact pressures, we demonstrate that the current SSAs can produce $\Delta R_{contact}$ > 100 kΩ (Figure 3c and Movie S6, Supporting Information). A plot of ΔR versus time recorded for all sensors during the study is provided in Figure 3d. The grabbing sequence involves applying an inflation pressure of 83 kPa for 15s, followed by an increase of the inflation pressure to 165 kPa for 30 s. Note that $\Delta R_{contact}$ increases at this inflation pressure even without an object was in its grasp. When grabbing the smooth object, $\Delta R_{contact}$ is ≈40 kΩ at 165 kPa, ≈30% higher than when grabbing nothing. $\Delta R_{contact}$ reached 300–500 kΩ when grabbing the spiked object, whose texture generated higher contact pressures.

Next, we explored temperature sensing using these SSAs. The ionogel conductivity as a function of temperature is given by the Vogel–Tamman–Fulcher equation[37,42]

$$\sigma = \rho^{-1} = \alpha \cdot \exp\left[-\frac{\beta}{(T - T_0)}\right] \quad (1)$$

where σ is conductivity, T is temperature, and α, β, and T_0 are fitting parameters. Hence, the printed sensor R should decrease with increasing T according to

$$R = \left(\frac{L}{A}\right)\left(\alpha \cdot \exp\left[-\frac{\beta}{(T - T_0)}\right]\right)^{-1} = \alpha^* \cdot \exp\left[\frac{\beta}{(T - T_0)}\right] \quad (2)$$

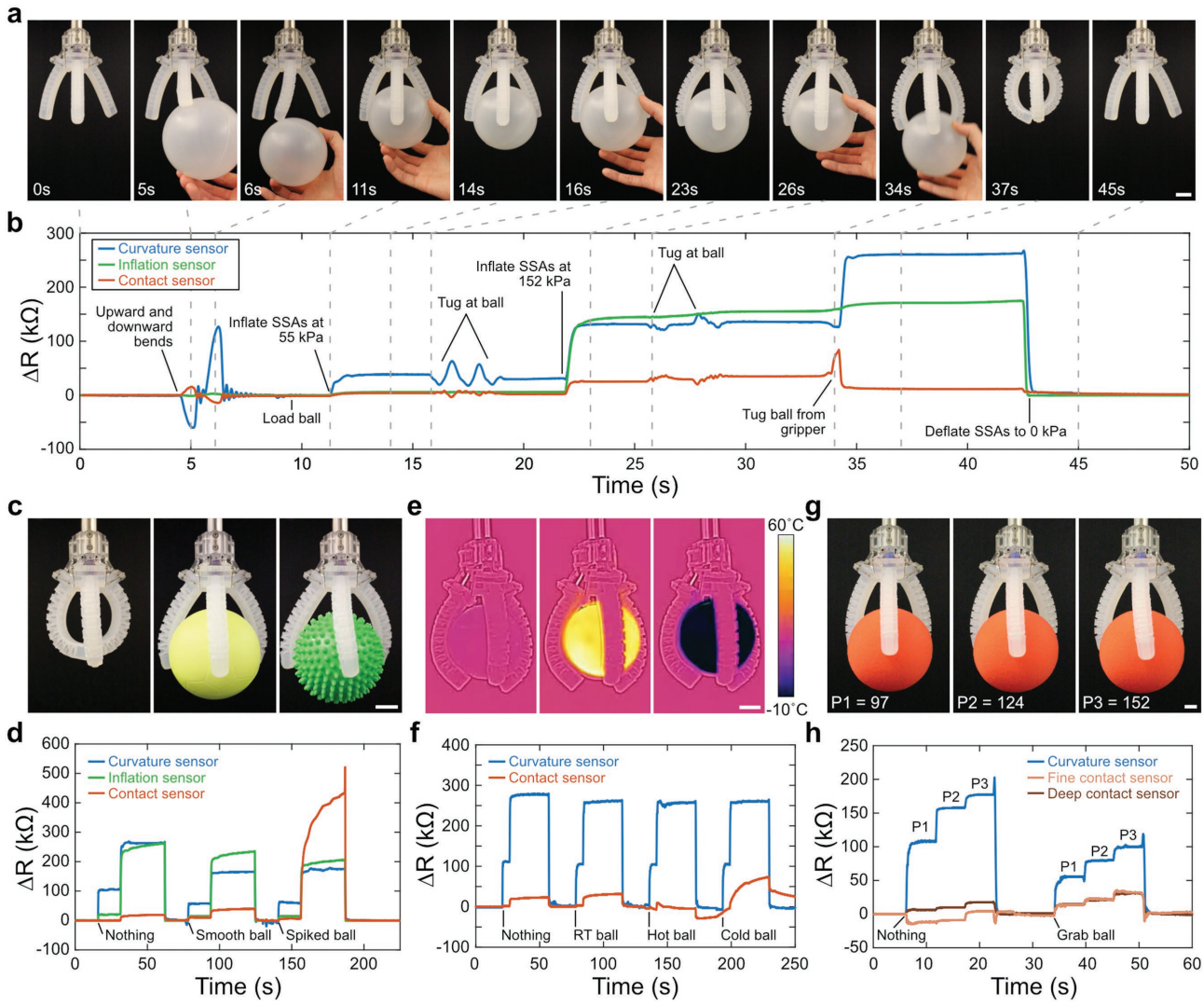

Figure 3. Soft robotic grippers with somatosensory feedback. a) Images of an interaction sequence between a ball and a soft robotic gripper comprised of SSAs (see Movie S5 in the Supporting Information; scale bar is 20 mm). b) ΔR of each sensor as a function of time during the interaction sequence shown in (a). (Note: The noninflated gripper ($t = 0$ s) had one SSA bent upward ($t = 5$ s) and downward ($t = 6$ s) before the ball is inserted into the gripper. The gripper is then inflated to 55 kPa ($t = 11$ s) to hold the ball ($t = 14$ s) even when manually tugged ($t = 16$ s). The inflation pressure is increased to 152 kPa for a stronger grip ($t = 23$ s). After additional tugging ($t = 26$s), the ball is removed from the gripper ($t = 34$ s), which remains inflated at 152 kPa ($t = 37$ s). The gripper is deflated at $t \approx 43$ s.) c) Still images show the gripper holding nothing (left), a smooth ball (middle), and a spiked ball (right) (see Movie S6 in the Supporting Information; scale bar is 20 mm). d) ΔR for each sensor is plotted as a function of time. e) Thermal images of a gripper holding a room temperature (RT) ball, a hot ball (≈60 °C), and a cold ball (≈0 °C) (see Movie S7 in the Supporting Information; scale bar is 20 mm). f) $\Delta R_{curvature}$ and $\Delta R_{contact}$ plotted as a function of time. g) Still images showing a gripper comprised of SSAs with embedded fine and deep contact sensors holding a foam ball at 97 kPa (P1), 124 kPa (P2), and 152 kPa (P3) (see Movie S9 in the Supporting Information; scale bar is 10 mm). h) The $\Delta R_{curvature}$, ΔR_{fine}, and ΔR_{deep} are plotted as a function of time for the sequence shown in (g).

We first validated this behavior over $T = 5$–95 °C (Figure S10a, Supporting Information) and then used the soft robotic gripper to grab three identical plastic balls held at room temperature (RT), ≈60 °C (hot), or ≈0 °C (in dry ice, cold) by inflating the gripper to 83 kPa for 15 s then at 165 kPa for 30 s (Figure 3e and Movie S7, Supporting Information). ΔR is plotted as a function of time in Figure 3f for these conditions. When grabbing the RT ball at 165 kPa, $\Delta R_{contact}$ is ≈9 kΩ greater than that for when the gripper holds nothing at 165 kPa. When grabbing the hot ball, $\Delta R_{contact}$ decreases noticeably, even becoming negative, due to the local increase in the contact sensor's conductivity where the distal meander made contact with the ball. Finally, when grabbing the cold ball, a clear increase in $\Delta R_{contact}$ is observed that exceeds the value of $\Delta R_{contact}$ for the same ball held at RT. When the gripper releases the hot and cold balls, $\Delta R_{contact}$ does not immediately return to the value of 0 kΩ measured at RT. Note, in this current embodiment, our SSAs cannot readily decouple the contact pressure and temperature of arbitrary objects in a straightforward manner. To optimize these dual sensing modalities in future SSAs, we could either add new sensors composed of alternate conductive materials or implement machine learning approaches by acquiring large

sets of training data during grasping objects of varying size, shape, surface texture, and temperature.

As a final demonstration, we created SSAs with both fine and deep contact sensors, which are printed with identical widths of the original contact sensor, but with shorter lengths and at different heights within the anterior matrix (the fine contact sensor is positioned closer to the surface of the anterior matrix) (Figure S10b, Supporting Information). Importantly, in this dual design, ΔR of the fine contact sensor in response to an applied contact pressure is higher than that observed for the deep contact sensor (Figure S10c, Supporting Information). The fine and deep contact sensors also have different receptive fields, akin to human fingers (see Movie S8 and Figure S10d,e in the Supporting Information). To illustrate this, a soft foam ball is grabbed at three different inflation pressures, 97 kPa (P1), 124 kPa (P2), and 152 kPa (P3) (Figure 3g). ΔR for the fine (ΔR_{fine}) and deep (ΔR_{deep}) contact sensors are provided in (Figure 3h) for these conditions, alongside a control experiment in which the gripper grabs nothing (Movie S9, Supporting Information). For each inflation pressure, ΔR_{fine} is negative or ≈0 kΩ when the gripper grabs nothing and increases noticeably when grabbing the ball. The deep contact sensor is less sensitive, but ΔR_{deep} is still ≈8, 10, and 12 kΩ greater when grabbing the ball at P1, P2, and P3, respectively, than when grabbing nothing. The ability to integrate multiple contact sensors sensitive to different modes of contact may facilitate handling of extremely delicate objects.

In summary, we have shown that our EMB3D printing method and accompanying materials palette enable the construction of soft robotic actuators with conductive features that emulate the human somatosensory system. By embedding multiple sensor networks within a molded elastomeric matrix, we created soft robotic actuators with haptic, proprioceptive, and thermoceptive sensing. The sensors consist of a conductive ionogel that is both stable long term and hysteresis free, while the pervasive pneumatic channels that drive their actuation when inflated are patterned using a fugitive ink. Our approach represents a foundational advance that may find potential application in soft robotic, wearable, and haptic devices[45] requiring embedded soft sensing for closed-loop control.

Experimental Section

Materials: Three matrix (dorsal, actuator, and anterior) materials and two (sensor and fugitive) inks were used to create SSAs by EMB3D printing. All matrix materials were formulated from commercially available two-part, platinum-cure silicone elastomers and compatible cure retarder (Slo-Jo) and thickener (Thivex) (all from Smooth-On Inc., USA). The dorsal matrix was prepared by mixing Parts A and B of Ecoflex 00–10 in a 1:1 ratio with 1.2 w/w% Slo-Jo and 0.6 w/w% Thivex (both with respect to Part B). The actuator matrix was prepared by mixing Parts A and B of SortaClear 40 in a 10:1 ratio with 2 w/w% Slo-Jo and 0.15 w/w% Thivex (both with respect to Part A). The anterior matrix was prepared by mixing Parts A and B of Ecoflex 00–30 in a 1:1 ratio with 1.5 w/w% Slo-Jo and 1.2 w/w% Thivex (both with respect to Part B). The sensor ink is a 6 wt% suspension of Aerosil 380 fumed silica (Evonik, USA) in EMIM-ES (≥95%, Sigma-Aldrich, USA). The fugitive ink is a 25 wt% suspension of physically gelled Pluronic F127 (Sigma-Aldrich, USA) in deionized, ultrafiltrated water. Further details are provided in the Supporting Information.

Rheological Characterization: The rheological properties of the matrix materials and inks were measured using a stress-controlled rheometer (DHR-3, TA Instruments, New Castle, DE, USA) equipped with a 40 mm diameter, 2° cone geometry. All measurements were carried out at room temperature (21 °C) after a stationary equilibration phase of 10 or 1 min for the matrix materials and inks, respectively. The 10 min equilibration time was selected to simulate the time between matrix material preparation and ultimate EMB3D printing and allow these thixotropic materials to reach steady-state rheological behavior. For oscillatory strain sweeps, the shear storage (G') and loss (G'') moduli were measured at a frequency of 1 Hz. Additional details regarding the measurement of matrix thixotropy are provided in the Supporting Information.

SSA Fabrication: A custom-designed, multimaterial 3D printer (ABG 10000, Aerotech Inc., Pittsburg, PA, USA) equipped with four independently addressable *z*-axis stages was used to fabricate the SSAs.[14,41] All G-Code for EMB3D printing was generated from Python-based software developed in-house.[14] After printing was complete, the matrix materials were crosslinked and each SSA was removed from the mold assembly. The SSAs were cooled to 4 °C for ≈1 h, and the liquefied fugitive ink was removed. A stainless steel nozzle with Luer lock fixture and electrical leads were inserted through the actuator matrix into the inlets to the actuator network and all sensors, respectively. (See the Supporting Information for additional details.)

SSA Characterization: Based on prior strategies for measuring the resistance, R, of ionically conductive soft sensors,[29] the read-out electronics are shown in Figure S5 (Supporting Information) to measure R for each EMB3D printed sensor. A relaxation oscillator using a low-voltage inverting operational amplifier was used to pass an oscillatory voltage in the form of a square wave across a printed sensor (Figure S5, Supporting Information). ΔR was calculated from changes in the period of this signal, which was acquired using an NI USB-6212 16-bit data acquisition unit (National Instruments, Austin, TX, USA), using MATLAB (see the Supporting Information).

To study the influence of relative humidity (RH) of sensor resistance, 21 strain sensors were printed into 3 mm deep molds filled with the anterior matrix material, cured in a 90 °C oven overnight, and had their resistances measured. For these sensors, $R_0 = 1186 \pm 134$ kΩ ($n = 21$) at day 0. Batches of seven sensors were kept at one of the three different conditions: on a laboratory bench top with RH of 53 ± 2%, in a dry box with RH = 27 ± 2%, and in a tissue culture incubator at a temperature of 37 °C and RH = 85%. The R of each sensor was measured at days 1, 2, 4, 6, 8, 14, and 20. After the day 20 measurement, the sensors were kept in a 90 °C oven, and R measurements were taken on day 21 and day 25 of the experiment, corresponding to 1 and 5 d in the 90 °C environment. Before taking any measurements, the sensors were kept on a laboratory bench top for 30 min.

Before any data acquisition or general use, SSAs underwent three break-in cycles to remove any influences on actuator or sensor performance arising from the Mullins effect. A break-in cycle for an SSA involved inflating to 14 kPa for 20s, deflating for 20s, inflating to a 28 kPa, and so on, increasing the inflation pressure in 14 kPa increments until a final inflation pressure of 152 kPa was used. Inflation was achieved using pressure regulation from 800 Ultra fluid dispensing systems (EFD Inc., East Providence, RI, USA).

During free and blocked displacement characterization, SSAs were inflated over the pressure range of 0–152 kPa. SSAs were inflated for 30 s at a given inflation pressure, resistance measurements were recorded for each sensor (taken as the mean R over a 3 s sampling interval), and the inflation pressure was increased/decreased by 14 kPa. For free displacement characterization, photographs were taken during each measurement, and the displacement angle of the SSA tip was measured in ImageJ image analysis software (NIH.gov). For blocked displacement characterization, SSAs were inflated against a mass balance. Force generated by the SSA was calculated as the product of the mass recorded on the mass balance and acceleration due to gravity. Figure S7a,b (Supporting Information) shows the free and blocked displacement characterization setups.

For contact sensor characterization, a translation stage (i.e., a *z*-axis on the multi-material printer) was used to generate a contact pressure against the contact sensor's distal meander while the SSA was laid on the mass balance upside-down (see Figure S7c in the Supporting Information). An acrylic rectangle was laser cut with dimensions covering the area of the contact sensor's distal meander and glued to

a Luer lock assembly that was fixed to our translation stage. A ≈2 mm thick piece of cured anterior matrix with the same dimensions as the acrylic rectangle separated the acrylic rectangle and the SSA to eliminate any stress concentration effects. Using the stage, the acrylic part was pressed into the contact sensor at 0.2 mm increments, generating contact pressures (calculated as the product of the measured mass and acceleration due to gravity divided by the area of the acrylic rectangle). Resistance measurements were recorded at each increment (taken as the mean R over a 3 s sampling interval). Identical methods were used to characterize the fine and deep contact sensors, which used rigid acrylic parts sized to the areal dimensions of each sensor.

To characterize the temperature-induced changes in sensor R, a strain sensor was placed on the Peltier plate of the DHR-3 rheometer (set at 20 °C). The temperature was kept constant for 60 s before R was recorded (taken as the mean R over a 3 s sampling interval). Without removing the sensor, the temperature was changed to 5 °C, R was recorded, and this process continued in 5 °C increments over the temperature range of 5–95 °C in 5 °C increments.

Gripper Assembly Design and Fabrication: To form the soft robotic gripper, three individual SSAs were mounted in a triangle shaped configuration and tethered to compressed air regulators (EFD Inc., East Providence, R.I., USA) and readout electronics. Actuator mounts were laser cut from acrylic on a VersaLaser PLS6.75 CO_2 laser (Universal Laser Systems, USA) and manually formed using a heat gun and hand tools. The mount adapter was CNC machined using a Haas OM-2A vertical machining center (Haas Automation Inc., USA). Three SSAs were first fastened into actuator mounts and then onto the mount adapter. All tethers to the compressed air regulators and readout electronics were threaded through the hollow tube on which the mount adapter was held. All hardware and raw materials were purchased from McMaster-Carr Supply Co., USA.

Imaging and Videography: Photographs and supporting videos were taken with a digital SLR camera (Canon EOS 5D Mark II, Canon USA Inc). Supporting micrographs were taken with a digital zoom microscope (VHX-2000, Keyence, Japan). An IR camera (FLIR T621, FLIR Systems Inc.) was used to record thermal videos during gripper grab tests. Video sequences were clipped from raw footage and exported using iMovie (Apple Corp, USA), and all photographs and still shots taken from videos were cropped using Affinity Designer vector graphics editor (www.affinity.serif.com/en-us/designer, Serif Europe Ltd).

Supporting Information

Supporting Information is available from the Wiley Online Library or from the author.

Acknowledgements

The authors thank A.D. Valentine and J.T. Muth for their valuable input and L.K. Sanders for assistance with photography and videography. The authors gratefully acknowledge support from the National Science Foundation through the Harvard MRSEC (DMR-1420570) and the Wyss Institute for Biologically Inspired Engineering. R.L.T. acknowledges support from a National Science Foundation Graduate Research Fellowship. J.A.L. acknowledges support from the Vannevar Bush Faculty Fellowship Program sponsored by the Basic Research Office of the Assistant Secretary of Defense for Research and Engineering and funded by the Office of Naval Research Grant N00014-16-1-2823, as well as the generous donation from the GETTYLAB in support of this work.

Conflict of Interest

Jennifer A. Lewis is a co-founder of Voxel8, a multimaterial 3D printing company that has spun out of the author's lab at Harvard University.

Keywords

3D printing, haptics, ionogels, soft robotics, soft sensors

Received: November 2, 2017
Revised: December 13, 2017
Published online:

[1] D. Rus, M. T. Tolley, *Nature* **2015**, *521*, 467.
[2] C. Laschi, B. Mazzolai, M. Cianchetti, *Sci. Robot.* **2016**, *1*, eaah3690.
[3] E. Brown, N. Rodenberg, J. Amend, A. Mozeika, E. Steltz, M. R. Zakin, H. Lipson, H. M. Jaeger, *Proc. Natl. Acad. Sci. USA* **2010**, *107*, 18809.
[4] J. Hughes, U. Culha, F. Giardina, F. Guenther, A. Rosendo, F. Iida, *Front. Robot. AI* **2016**, *3*, https://doi.org/10.3389/frobt.2016.00069.
[5] J. Morrow, H. S. Shin, C. Phillips-Grafflin, S. H. Jang, J. Torrey, R. Larkins, S. Dang, Y. L. Park, D. Berenson, in *IEEE Int. Conf. on Robotics and Automation (ICRA, IEEE)*, IEEE, Piscataway, NJ, USA **2016**, pp. 5024–5031.
[6] H. Zhao, K. O'Brien, S. Li, R. F. Shepherd, *Sci. Robot.* **2016**, *1*, eaai7529.
[7] M. Wehner, B. Quinlivan, P. M. Aubin, E. Martinez-Villalpando, M. Baumann, L. Stirling, K. Holt, R. Wood, C. Walsh, in *IEEE Int. Conf. on Robotics and Automation (ICRA, IEEE)*, IEEE, Piscataway, NJ, USA **2013**, pp. 3362–3369.
[8] Y.-L. Park, B. Chen, N. O. Pérez-Arancibia, D. Young, L. Stirling, R. J. Wood, E. C. Goldfield, R. Nagpal, *Bioinspiration Biomimetics* **2014**, *9*, 16007.
[9] H. Zhao, J. Jalving, R. Huang, R. Knepper, A. Ruina, R. Shepherd, *IEEE Robot. Autom. Mag.* **2016**, *23*, 55.
[10] A. D. Marchese, C. D. Onal, D. Rus, *Soft Robot.* **2014**, *1*, 75.
[11] M. T. Tolley, R. F. Shepherd, B. Mosadegh, K. C. Galloway, M. Wehner, M. Karpelson, R. J. Wood, G. M. Whitesides, *Soft Robot.* **2014**, *1*, 213.
[12] T. Li, G. Li, Y. Liang, T. Cheng, J. Dai, X. Yang, B. Liu, Z. Zeng, Z. Huang, Y. Luo, T. Xie, W. Yang, *Sci. Adv.* **2017**, *3*, e1602045.
[13] D. Drotman, S. Jadhav, M. Karimi, P. DeZonia, M. T. Tolley, in *IEEE Int. Conf. on Robotics and Automation (ICRA, IEEE)*, IEEE, Piscataway, NJ, USA **2017**, pp. 5532–5538.
[14] M. Wehner, R. L. Truby, D. J. Fitzgerald, B. Mosadegh, G. M. Whitesides, J. A. Lewis, R. J. Wood, *Nature* **2016**, *536*, 451.
[15] C. D. Onal, X. Chen, G. M. Whitesides, D. Rus, in *Robotics Research, Springer Tracts in Advanced Robotics*, Vol. *100*, (Eds.: H. I. Christensen, O. Khatib), Springer, Cham, Switzerland **2017**, pp. 525–540.
[16] T. Buschmann, B. Trimmer, in *Neurobiology of Motor Control: Fundamental Concepts and New Directions*, (Eds: S. L. Hooper, A. Büschges), John Wiley & Sons, Inc., Hoboken, NJ, USA **2017**.
[17] K. Kure, T. Kanda, K. Suzumori, S. Wakimoto, in *IEEE Int. Conf. on Robotics and Automation (ICRA, IEEE)*, IEEE, Piscataway, NJ, USA **2006**, pp. 1012–1017.
[18] Y. L. Park, R. J. Wood, in *2013 IEEE Sensors (IEEE)*, IEEE, Piscataway, NJ, USA **2013**, pp. 1–4.
[19] S. S. Robinson, K. W. O'Brien, H. Zhao, B. N. Peele, C. M. Larson, B. C. Mac Murray, I. M. Van Meerbeek, S. N. Dunham, R. F. Shepherd, *Extreme Mech. Lett.* **2015**, *5*, 47.
[20] R. Adam Bilodeau, E. L. White, R. K. Kramer, in *IEEE Int. Conf. on Intelligent Robots and Systems (IROS, IEEE)*, IEEE, Piscataway, NJ, USA **2015**, pp. 2324–2329.
[21] C. Larson, B. Peele, S. Li, S. Robinson, M. Totaro, L. Beccai, B. Mazzolai, R. Shepherd, *Science* **2016**, *351*, 1071.
[22] J. C. Yeo, H. K. Yap, W. Xi, Z. Wang, C.-H. Yeow, C. T. Lim, *Adv. Mater. Technol.* **2016**, *1*, 1600018.

[23] B. S. Homberg, R. K. Katzschmann, M. R. Dogar, D. Rus, in *IEEE Int. Conf. on Intelligent Robots and Systems (IROS, IEEE)*, IEEE, Piscataway, NJ, USA **2015**, pp. 1698–1705.
[24] Z. Wang, S. Hirai, in *Proc. 2016 IEEE/SICE Int. Symp. System Integration (IEEE)*, IEEE, Piscataway, NJ, USA **2017**, pp. 629–633.
[25] M. Luo, E. H. Skorina, W. Tao, F. Chen, S. Ozel, Y. Sun, C. D. Onal, *Soft Robot.* **2017**, *4*, 117.
[26] V. Wall, G. Zoller, O. Brock, in *IEEE Int. Conf. on Robotics and Automation (ICRA, IEEE)*, IEEE, Piscataway, NJ, USA **2017**, pp. 4965–4970.
[27] M. D. Dickey, *Adv. Mater.* **2017**, *29*, 1.
[28] S. Z. Guo, K. Qiu, F. Meng, S. H. Park, M. C. McAlpine, *Adv. Mater.* **2017**, *29*, 1.
[29] J. B. Chossat, Y. L. Park, R. J. Wood, V. Duchaine, *IEEE Sens. J.* **2013**, *13*, 3405.
[30] J. Y. Sun, C. Keplinger, G. M. Whitesides, Z. Suo, *Adv. Mater.* **2014**, *26*, 7608.
[31] H. Yuk, T. Zhang, G. A. Parada, X. Liu, X. Zhao, *Nat. Commun.* **2016**, *7*, 12028.
[32] T. Sekitani, Y. Noguchi, K. Hata, T. Fukushima, T. Aida, T. Someya, *Science* **2008**, *321*, 1468.
[33] N. Matsuhisa, M. Kaltenbrunner, T. Yokota, H. Jinno, K. Kuribara, T. Sekitani, T. Someya, *Nat. Commun.* **2015**, *6*, 7461.
[34] W. Wu, A. Deconinck, J. A. Lewis, *Adv. Mater.* **2011**, *23*, H178.
[35] J. T. Muth, D. M. Vogt, R. L. Truby, Y. Mengüç, D. B. Kolesky, R. J. Wood, J. A. Lewis, *Adv. Mater.* **2014**, *26*, 6307.
[36] R. L. Truby, J. A. Lewis, *Nature* **2016**, *540*, 371.
[37] J. Vila, P. Ginés, J. M. Pico, C. Franjo, E. Jiménez, L. M. Varela, O. Cabeza, *Fluid Phase Equilib.* **2006**, *242*, 141.
[38] R. Di Giacomo, L. Bonanomi, V. Costanza, B. Maresca, C. Daraio, *Sci. Robot.* **2017**, *2*, eaai9251.
[39] J.-B. Chossat, H.-S. Shin, Y.-L. Park, V. Duchaine, *J. Mech. Robot.* **2015**, *7*, 21008.
[40] J. B. Chossat, Y. Tao, V. Duchaine, Y. L. Park, in *IEEE Int. Conf. on Robotics and Automation (ICRA, IEEE)*, IEEE, Piscataway, NJ, USA **2015**, pp. 2568–2573.
[41] D. B. Kolesky, R. L. Truby, A. S. Gladman, T. A. Busbee, K. A. Homan, J. A. Lewis, *Adv. Mater.* **2014**, *26*, 3124.
[42] E. Rilo, J. Vila, S. García-Garabal, L. M. Varela, O. Cabeza, *J. Phys. Chem. B* **2013**, *117*, 1411.
[43] Y. L. Park, B. R. Chen, R. J. Wood, *IEEE Sens. J.* **2012**, *12*, 2711.
[44] Y. L. Park, D. Tepayotl-Ramirez, R. J. Wood, C. Majidi, *Appl. Phys. Lett.* **2012**, *101*, 191904.
[45] L. Yao, R. Niiyama, J. Ou, S. Follmer, C. Della Silva, H. Ishii, in *Proc. 26th Annual ACM Symp. on User Interface Software and Technology (ACM)*, ACM, New York **2013**, pp. 13–22.